Dynamic procedure for daily PM56 ETo mapping conducive to site-specific irrigation recommendations in areas covered by agricultural weather networks

A. Garcia-Prats [a,*], J.M. Carricondo-Anton [a], M.A. Jiménez-Bello [a], J. Manzano Juárez [b], E. López-Pérez [a], M. Pulido-Velazquez [a]

[a] Research Institute of Water and Environmental Engineering (IIAMA), Universitat Politècnica de València, Camino de vera s/n, 46022 Valencia, Spain
[b] Centro Valenciano de Estudios sobre el Riego (CVER), Universitat Politècnica de València, Camino de vera s/n, 46022 Valencia, Spain

ARTICLE INFO

ABSTRACT

Modern agriculture is underpinned by actual meteorological data registered using automated meteorological stations forming networks specifically created for advising purposes. In many cases, those data used to be accessible online by means of APIs (Application Programming Interface). One of the most common cases is the irrigation-advice weather network implemented with the aim of obtaining ETo values to be used in irrigation recommendations. However, those punctual values of ETo scattered throughout the territory do not allow to produce specific irrigation recommendations for each farm. The only way of disposing site-specific values of ETo is by compiling maps that describe its spatial variation. With this objective, a new dynamic procedure based on an existing regression-based technique of interpolation was proposed. Using the meteorological data registered at the end of each day, maximum and minimum temperature, maximum and minimum relative humidity, wind velocity, and radiation maps were interpolated and then, an ETo map was derived. The proposed procedure demonstrated a special adaptation capacity to the synoptic pattern of each day using some geographical features or others, as appropriate to explain the spatial variability of the interpolated meteorological variable. In those months where radiation plays a key role in the ETo value (growing season), ETo maps obtained were especially fine-grained in areas with significant relief. This procedure improved other contrasted methodologies they were compared with. The impact of using the nearest-weather-station ETo vs interpolated value on a daily water needs was investigated and near 10% average value of error was encountered in the case study.

1. Introduction

In recent times, a multitude of agricultural weather networks (AWN) have been developed around the world with the aim of advising agricultural activities (Shulski et al., 2018) certainly fostered by the exponential growth of digital technologies. Few years ago, the installation and maintenance of these kinds of facilities were only within reach of governmental agencies and national weather services of countries. However, nowadays cooperative extensions, universities, growers' associations, and regional or even local governments are providing this service thanks to the automated weather stations. Furthermore, adopting modern information and communication technologies allows data to be available in real-time. Among the different ways of serving the registered data to the users, weather APIs (Application Programming Interface) are gaining space due to their flexibility. Any authorized user can retrieve data online from the AWN creating software applications that directly consume the data. In this sense, it is worth to highlight the increase of the AWNs specifically set up to advice irrigators (Elliott et al., 2000). This type of weather station uses to be equipped with enough sensors (temperature and relative humidity probes, anemometer, and pyranometer) to derive the FAO-56 Penman-Monteith (PM56) reference evapotranspiration (ETo) (Brown, 2007) as an expression of the daily evaporative demand of the atmosphere (Raes et al., 2009). ETo along with the registered rainfall allows to provide irrigation recommendations using the FAO-56 methodology (Allen et al., 1998).

Nonetheless, even if an irrigation-advice weather network exists in a region, stations density does not allow producing specific irrigation recommendations for each farm. Depending on the relative location of
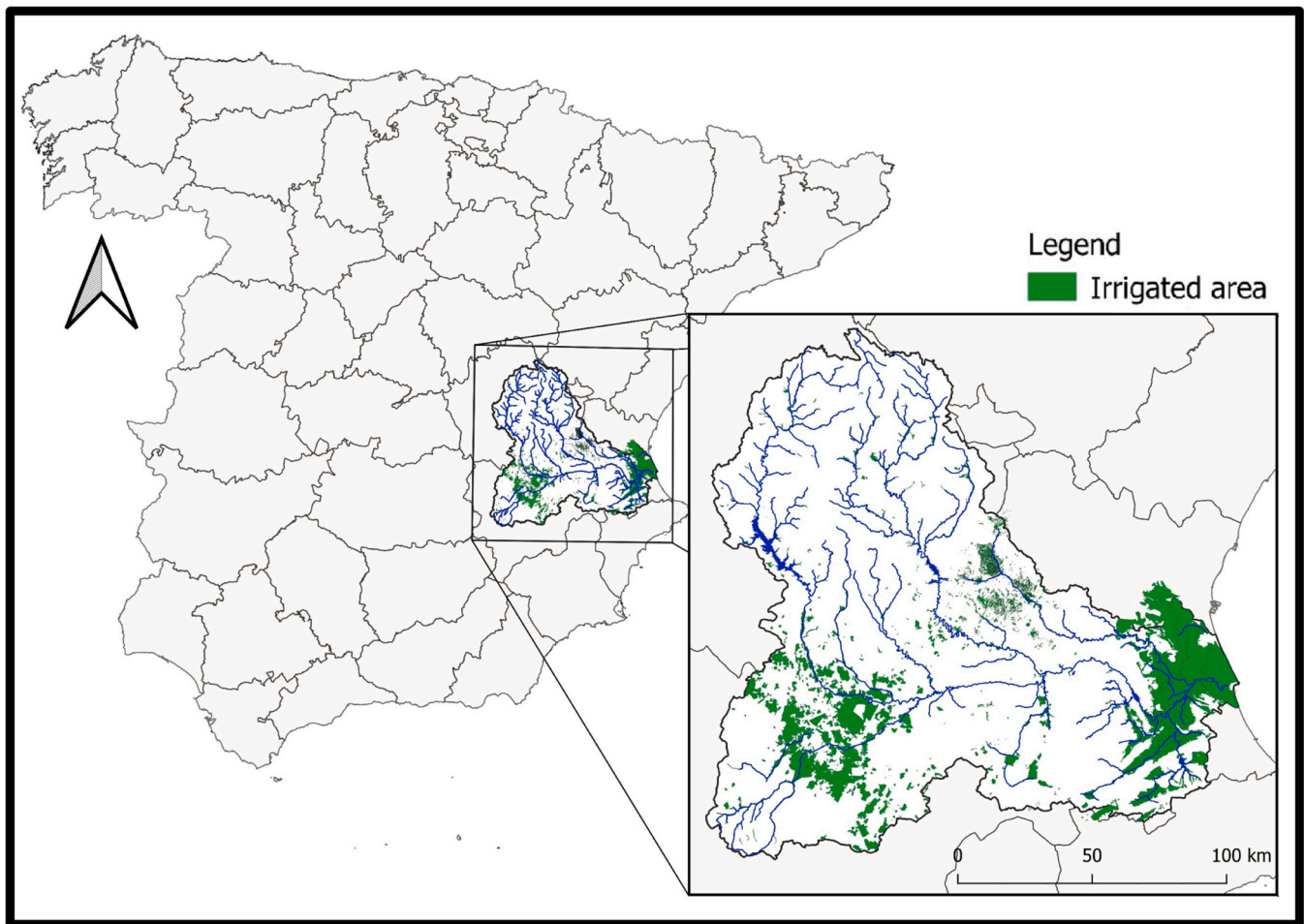

Fig. 1. Jucar River system location.

the farm in respect of the weather station, the ETo employed could come from many kilometers apart (Martínez-Lüscher et al., 2022). Under this circumstance, the only way of disposing site-specific values of ETo is by compiling maps that describe its spatial variation (Vicente-Serrano et al., 2007). To do that, two main procedures can be identified in the literature. On the one hand, a number of authors employed geostatistical or deterministic interpolation methods: Hodam et al. (2017), Mancosu et al. (2014), Noshadi and Sepaskhah (2005), and Martinez-Cob (1996) utilized ordinary kriging, residual kriging, cokriging and inverse distance squared. Martínez-Cob and Cuenca (1992) and Mardikis et al. (2005) proposed variations in some of them to include the terrain elevation as a covariate due to its deep influence in landscapes with some relief. On the other hand, and considering that ETo would be spatially influenced by not only elevation but other geographical features, other authors opted for statistical techniques of mapping previously employed successfully to map other meteorological variables like temperature (Agnew and Palutikof, 2000; Ninyerola et al., 2007a), precipitation (Daly et al., 2002; Ninyerola et al., 2007b) or radiation (Pons and Ninyerola, 2008). This kind of interpolation method uses to be based on multiple linear regressions in which the explained meteorological variable is related to some geographical characteristic like latitude, longitude, elevation, continentality, slope, aspect, etc. acting as independent variables. To date, only a few studies have explicitly addressed this ETo-mapping approach. Furthermore, the existing ones are obtained on a monthly basis (Vicente-Serrano et al., 2007; McVicar et al., 2007), a definitely time-step not valid to be used to make irrigation recommendations that need at most weekly or preferably daily ETo values.

It is worth emphasizing that the aforementioned regression-based statistical techniques of mapping ETo can be addressed under two different headings (McVicar et al., 2007): i) "calculate-then-interpolate approach", interpolating directly the punctual ETo values obtained in each weather station on the region covered for the AWN (Martí and Zarzo, 2012), or ii) "interpolate-then-calculate" approach, interpolating separately each meteorological variable involved in the PM56 formulation (maximum and minimum temperature, maximum and minimum relative humidity, 2-meter height wind speed and solar radiation) and then applying layer algebra for each grid-cell to derive the ETo map (Vicente-Serrano et al., 2007; McVicar et al., 2007). As a general rule, in the previous monthly-basis works, authors agreed that better results were obtained using the second approach despite the error propagation along with each interpolation involved (Vicente-Serrano et al., 2007). Conversely, from a temporal point of view, those previous monthly-basis-works are "static", due to the fact that the regression coefficients were obtained using a certain weather-station percentage of the network, and validated in the rest of them (e.g. 80% mapping, 20% validation) but for the same period of time (e.g. same 15, 20 or whatever period of years). It is not proven that this approach guarantees the adequacy of these regression equations for a new period, i.e. for a new month of a new year, not to mention for producing daily ETo maps.

In relation to the generation of daily-meteorological-variable surfaces, a special mention deserves the contribution of (Thornton et al., 1997). They improved the MTCLIM logic model (Hungerford et al., 1989) applying a truncated Gaussian filter as an interpolation method and a weighted least-square regression between pairs of stations as a correction for the effect of the elevation on the variables. Using this
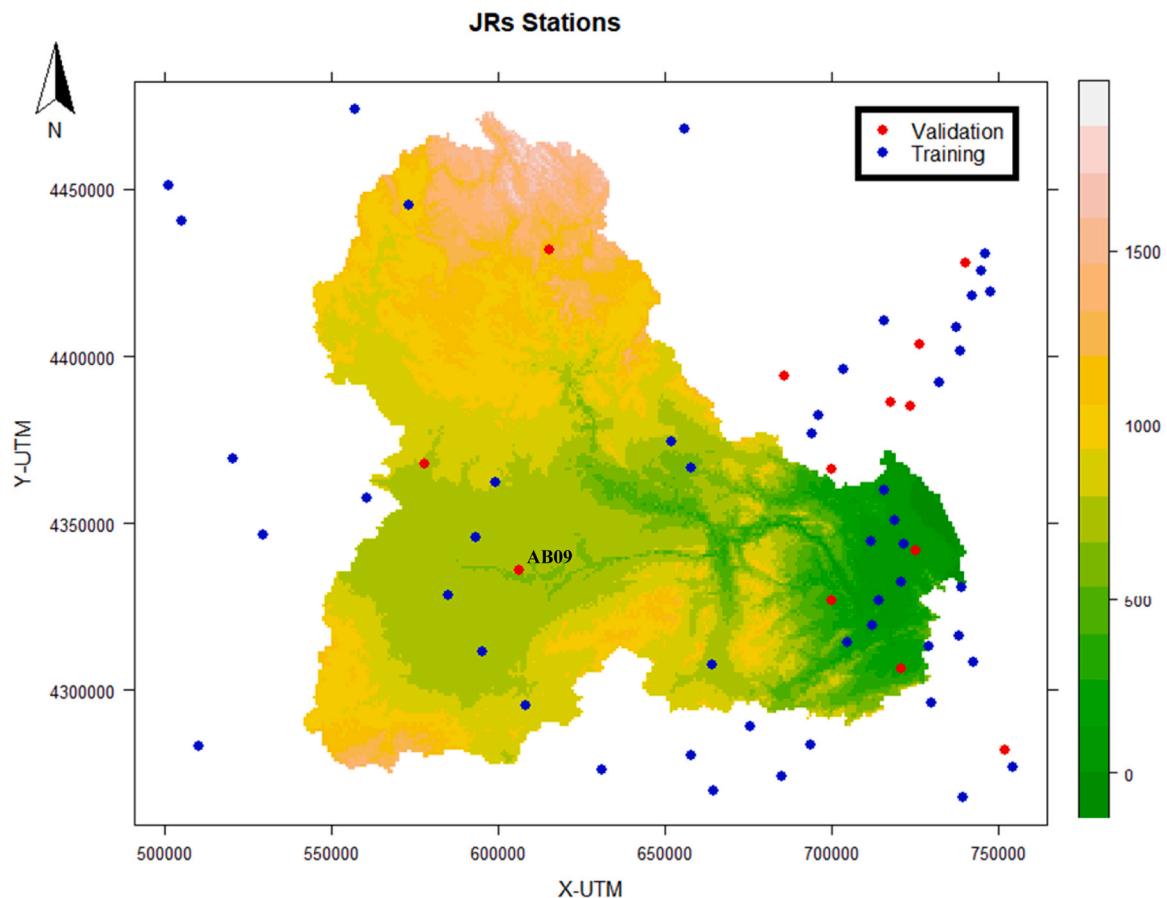
Fig. 2. Automated weather station of SIAR network locations and digital elevation model-DEM-of the JRs.

method, important products like DAYMET dataset (Oak Ridge National Laboratory, supported by NASA- USA) (Thornton et al., 2021, 1997) have been delivered. DAYMET dataset provides long-term, continuous, gridded estimates of daily weather and climatology variables on a 1 km x 1 km gridded surface over continental North America from 1980, but does not exist in other regions or in other resolutions. Using this same algorithm with a few modifications, the R package METEOLAND (De Cáceres et al., 2018) allows the spatial interpolation of daily weather records from meteorological stations in order to produce continuous surfaces. In this case, the user decides the spatial resolution by means of the resolution of the elevation surface or digital elevation model (DEM) employed in the interpolation procedure.

In regions covered by AWNs specifically devoted to irrigation-advice with weather-API-real-time access to the data, it is peremptory to investigate the development of a dynamic algorithm capable to obtain reliable ETo maps on a daily basis and with an adequate spatial resolution to produce site-specific irrigation recommendations and not just referred to the nearest weather station. At the end of each day, the API should serve a new map along with the regular daily meteorological records.

This study aims at contributing to an improved comprehension of ETo mapping on a daily basis considering the geographical characteristics of the landscape. Our study was conducted in the Jucar River system, a Mediterranean region of eastern Spain where the intensive irrigated agriculture and a pronounced relief in certain areas, provided an excellent context to address the following research questions (RQ):

RQ1:. Are monthly interpolation procedures capable to produce proper ETo maps on a daily basis using static equations coming from historical data?

RQ2:. Do all the meteorological variables involved in the PM56-ETo

calculation have the same influence on the final ETo value? And, Is this influence constant throughout the year?

RQ3:. Derived from the previous question, Does the lack of precision interpolating one meteorological variable have the same impact as another?

2. Material and methods

2.1. Case study area: the Jucar River system (JRs)

Placed in the east of Spain (Fig. 1), the Jucar River system (JRs) almost exactly matches the same-name river basin. According to the published information by the river authority (Confederación Hidrográfica del Júcar, 2022) the basin is characterized by a typical Mediterranean climate. The annual average precipitation is about 500 mm, ranging from 300 to 780 mm. The rainfall regime combines intense rains in autumn (October is the rainiest month with nearly 60 mm) and spring with dry summers (July is the driest month with nearly 13 mm). The average temperature ranges from 11 °C in winter to 26.6 °C in summer. The average ETo for the period 1980–2018 was 992.7 mm. The geographical area of the JRs is 2,226,093 ha of which 210,000 ha are irrigated. To finish with, citrus trees are the main crop occupying nearly 40% of the irrigated area, being cereals, vineyards, fruit trees, horticulture crops, and olives the other 60% (Confederación Hidrográfica del Júcar, 2022).

2.2. Meteorological data: "SIAR" agricultural weather network

Irrigated areas of the Jucar River system (JRs) are covered by the AWN named SIAR (Agro-climatic Information System for Irrigation
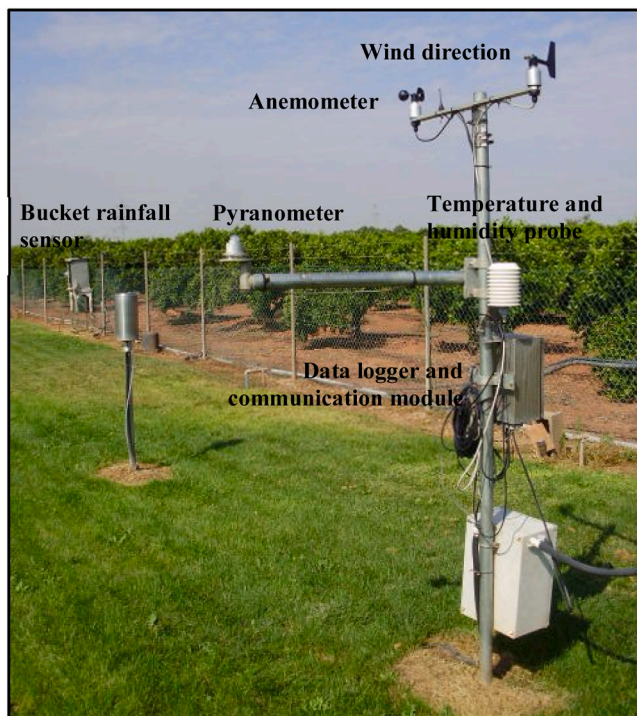
3

Fig. 3. Automated weather station of SIAR network.

-www.siar.es-). SIAR was created in 1998 to promote water savings by means of proper irrigation recommendations, and covering the main irrigable areas of Spain with a total of 460 automated weather stations, 63 of them located into or near the perimeter of the JRs, as can be seen in Fig. 2. SIAR was promoted by the Spanish Ministry of Agriculture, Fisheries and Food (MAPA), and is maintained -and in some cases densified with additional stations- by the different regional governments. That is the case of the JRs whose weather stations are maintained by the Valencian Community and Castile-La Mancha Community regional governments. In Fig. 3 can be seen a typical automated weather station equipped with a bucket rainfall sensor, anemometer, and wind direction located at 2 m-normalized high from the ground, temperature and humidity probes, and pyranometer. The station is completed with a data logger and a GSM communication module to transfer the data automatically several times a day. Meteorological records are registered every 30 min and then aggregated to hourly and daily data to be served through the API. In the stations of the SIAR network, preventive maintenance is carried out every six months, performing a general review. In the same way, an annual calibration of the station sensors is done in a laboratory. Corrective maintenance of any anomaly detected in the station is carried out.

2.3. Modeling framework

Since the final purpose of this work was developing a dynamic ETo mapping procedure to deliver site-specific irrigation recommendations according to FAO-56 methodology (Allen et al., 1998), the Penman-Monteith equation was adopted to calculate the reference evapotranspiration.

$$ETo = \frac{0.408 \cdot \Delta \cdot (R_n - G) + \gamma \cdot \frac{900}{T_m + 273} \cdot U_2 \cdot (e_s - e_a)}{\Delta + \gamma \cdot (1 + 0.34 \cdot U_2)}$$

Where *ETo* is the reference evapotranspiration (mm·d^{-1}); Δ is the slope vapour pressure curve (kPa ºC^{-1}); R_n is the net radiation at the crop surface (MJ m^{-2} día^{-1}); *G* is the soil heat flux density (MJ m^{-2} día^{-1}); U_2 is the wind speed at 2 m height (m s^{-1}); γ is the psychrometric constant

(kPa ºC^{-1}); $(e_s - e_a)$ is the saturation vapour pressure deficit (kPa); and T_m is the mean daily air temperature (ºC).

In this work, an "interpolate-then-calculate" approach was adopted. Thus, a continuous grid-cell map per meteorological variable involved in the PM56-ETo had to be previously interpolated, based on the daily records registered for the AWN. The spatial resolution of the grid-cell maps for all cases was 100 m.

Fig. 4 describes the proposed modeling framework. Three different spatial interpolation procedures were applied and then compared using model-performance metrics: i) Meteoland R package, ii) Monthly Static Regression-Based Interpolation (SRI), and iii) Daily Dynamic Regression-Based Interpolation (DRI). The three procedures are shortly described here, with some detail hereafter in the next section.

i) Meteoland (De Cáceres et al., 2018) R package implements, with few modifications, the daily weather interpolation algorithms developed by (Thornton et al., 2021, 1997) and (Thornton and Running, 1999) that underpin the DAYMET dataset (https://daymet.ornl.gov/). The interpolation procedure is based on a truncated Gaussian filter and the correction of the meteorological variables for the elevation effect is solved using a weighted least-square regression between stations and target points to be interpolated. Daily potential solar radiation is calculated after (Garnier and Ohmura, 1968) and the incident radiation after (Thornton and Running, 1999). Further details about the algorithms and procedures can be seen in De Cáceres et al. (2018) and the R package documentation (https://cran.r-project.org/web/-packages/meteoland/index.html). Meteoland was employed to interpolate 365 daily continuous surfaces (year 2022) of the mean (*Tm*), maximum (*Tmax*) and minimum (*Tmin*) temperature, maximum (*HRmax*) and minimum (*HRmin*) relative humidity, wind velocity (U_2) and incident solar radiation (*Rs*) using 49 training stations of SIAR network as defined in Fig. 2. Results were validated using 14 validation stations of the SIAR network as well as illustrated in Fig. 2. Finally, applying layer algebra for each grid-cell, the PM56-ETo map was obtained.

ii) Monthly Static Regression-Based Interpolation (SRI) is a regression-based procedure calculated using exactly the same methodology after Vicente-Serrano et al. (2007). Using a 15-year period (2007–2021), monthly multiple regression equations were obtained. Using those static monthly regression equations based on historical data, 365 daily for the year 2022 continuous grid-cell maps of *Tm, Tmax, Tmin, HRmax, HRmin,* and U_2 were obtained. An upward-looking hemispherical viewshed algorithm was employed to obtain *Rs* on a monthly basis. Finally, applying layer algebra for each grid-cell, the PM56-ETo map was derived. The same procedure of validation as described in the METEOLAND procedure was employed, explained in more detail in the next section.

iii) Daily Dynamic Regression-Based Interpolation (DRI). It turns out to be the very novelty proposal of this paper. Based on the SRI procedure, a new regression equation is obtained every day instead of using static regression equations obtained from historical data. According to the atmospheric conditions of each day, different geographical features are able to explain spatial variability. 365 daily continuous grid-cell maps for the year-2022 of *Tm, Tmax, Tmin, HRmax, HRmin, and* U_2 were obtained using this method. An upward-looking hemispherical viewshed algorithm was employed to get Rs on a daily basis. Finally, applying layer algebra for each grid-cell, the PM56-ETo map was derived. The same validation procedure described in the METEOLAND procedure was employed, explained in more detail in the next section.
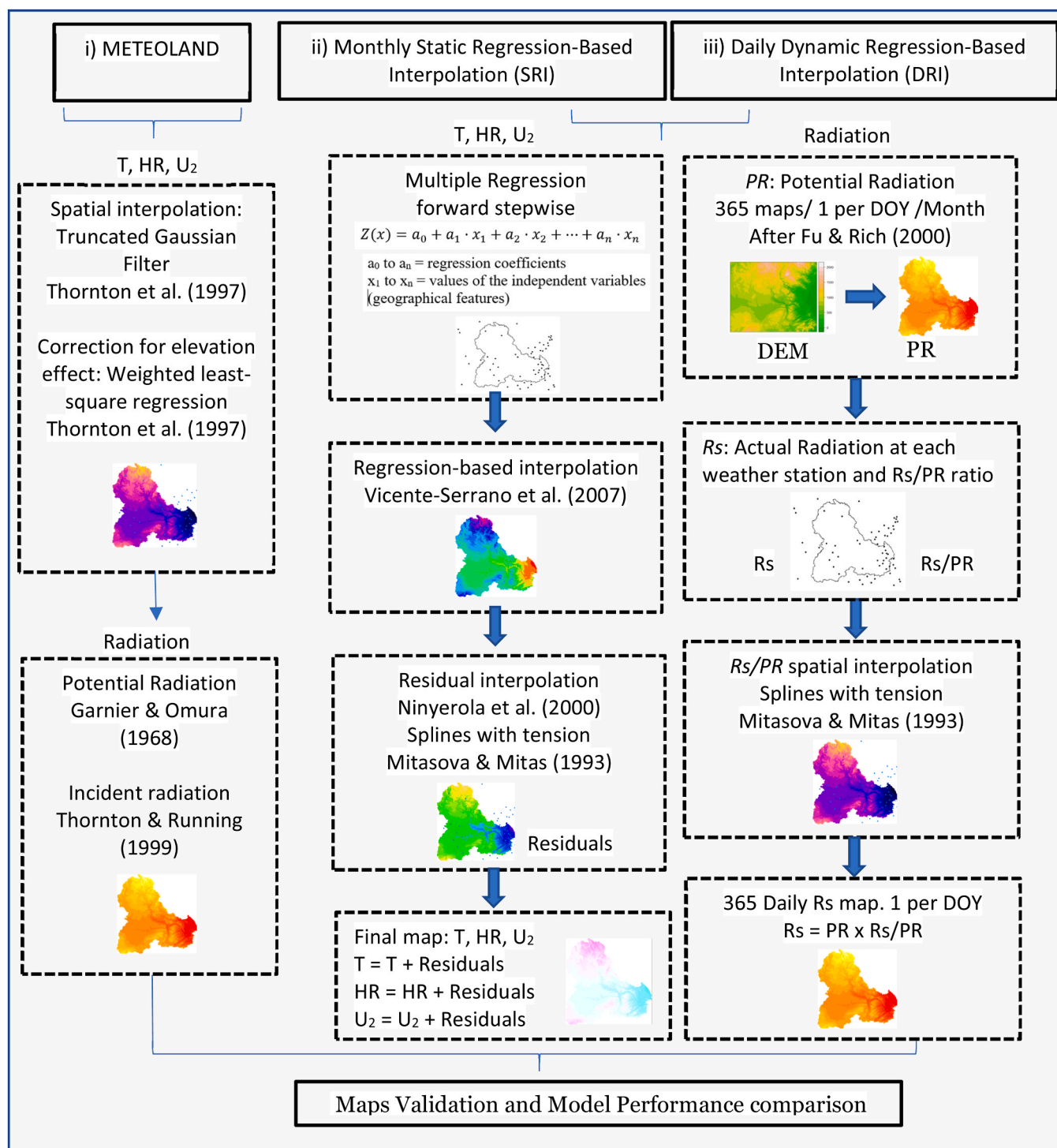
Fig. 4. Modeling framework. DOY = Day of the year (1−365), T = Temperature, HR = Relative humidity, U_2 = wind velocity. Other variables explained into the figure.

2.4. Monthly Static (SRI) and Daily Dynamic (DRI) regression-based interpolation procedures

2.4.1. Maximum and Minimum Temperature, Maximum and Minimum Relative Humidity and Wind Speed interpolation procedure

For this purpose, the regression-based technique of interpolation after Vicente-Serrano et al. (2007) and previously Ninyerola et al. (2000), was applied. The value of the variable in the space among weather stations was calculated using the equation:

$$Z(x) = a_0 + a_1 \cdot x_1 + a_2 \cdot x_2 + \ldots + a_n \cdot x_n$$

Where $Z(x)$ is the predicted value of the temperature, humidity, or wind speed, (°C, % or m·s^{-1} respectively); a_0 to a_n are the regression coefficients, and x_1 to x_n are the values of the independent variables (geographical features) at the spatial point x.

Table 1 includes the geographical features acting as independent variables. The linear relationship between them and the predicted temperature/humidity/wind speed was investigated using a multiple

Table 1
Geographical features acting as independent variables in the multiple regression interpolation.

LONG	Longitude, in degrees.
LAT	Latitude, in degrees.
MEDIT	Distance to the nearest sea with clear influence in the weather synoptic (the Mediterranean Sea in our case), in m.
RAD	Annual average incoming solar radiation, in MJ d^{-1}.
RADx	Annual average incoming solar radiation, in MJ d^{-1}, within x_i, where x is a radius of 2.5, 5, and 25 km.
ELEV	Elevation, in m.
ELEVx	Mean elevation, in m, within x_i, where x is a radius of 2.5, 5, and 10 km.
Slope	Terrain slope, in %.
Aspect	Terrain aspect, in 0–360 degrees, with respect north (0 degrees).

regression forward stepwise procedure. Only independent variables with $p_{value} < 0.01$ were included in the regression, avoiding collinearity problems derived from using the complete set (Hair et al., 2010). Homoscedasticity (using residual plots) and no residual autocorrelation (using the Durbin-Watson parameter) were checked as well.

After obtaining the geographical variables involved and the coefficients of the multiple regression equations, a continuous map was obtained by simply combining the raster layers with the information of each geographic variable and applying the algebraic formula. Logically, at the location of each weather station, the value of the registered and modeled temperature/humidity/wind speed does not match. Residuals use to be interpolated over the entire study area, and summed up to the predicted value using local techniques. In this case, the splines with tension method (Mitášová and Mitáš, 1993) was employed to do that. This way, registered and predicted values at the weather station locations employed to train the model (Training Stations in Fig. 2) coincide, and the validation in other locations improves substantially (Validation Stations in Fig. 2) according to Ninyerola et al. (2000) and Agnew and Palutikof (2000).

For SRI, monthly regression equations were obtained using a 15-year period of daily data (2007–2021). Those static monthly regression equations based on historical data were obtained only once and then employed in the generation of new daily continuous grid-cell maps of *Tm, Tmax, Tmin, HRmax, HRmin*, and *U$_2$* for the year-2022. Nevertheless, in DRI, based on the registered daily data along the AWN, a new regression equation was obtained specifically for each day. Only those geographical features with statical significance were included, being the case as they might be different even for two contiguous days.

2.4.2. Radiation interpolation procedure

Solar radiation plays a key role in the ET process due to the fact that is responsible of contributing the necessary energy to transform water

Table 2
Statistical metrics.

MAE	Mean absolute error	$MAE = \frac{1}{n}\sum_{j=1}^{n}\left|P_j - O_j\right|$
MBE	Mean bias error	$MBE = \frac{1}{n}\sum_{j=1}^{n}(P_j - O_j)$
RMSE	Root mean squared error	$RMSE = \sqrt{\frac{1}{n}\sum_{j=1}^{n}(P_j - O_j)^2}$
d	Index of Agreement (Willmott, 1982)	$d = 1 - \frac{\sum_{j=1}^{n}(P_j - O_j)^2}{\sum_{j=1}^{n}\left(\left|P_j - O_j\right| + \left|O_j - \overline{O}\right|\right)^2}$
NSE	Nash-Sutcliffe model efficiency (Nash and Sutcliffe, 1970)	$NSE = 1 - \frac{\sum_{j=1}^{n}(O_j - P_j)^2}{\sum_{j=1}^{n}(O_j - \overline{O})^2}$
Where:	P_j	Predicted values
	O_j	Observed values
	$\overline{O}$	Average of observed values
	n	Number of total values

from liquid to vapor state. Hence, the spatial heterogeneity of the incoming solar energy produced by a complex topography (elevation, slope, aspect and shadows) creates strong local gradients that determine the dynamic of the ET (Tovar-Pescador et al., 2006) that cannot be ignored assuming a flat terrain. For that reason, several models and almost all GIS platforms have developed algorithms for estimating solar radiation spatially-adapted to the relief: *SolarFlux* for ArcInfo (Dubayah and Rich, 1995), *Solar Analyst* for Arc View (Fu and Rich, 2000), SRAD (Wilson and Gallant, 2000), *Solei* for IDRISI (Miklánek, 1993), MiraMon GIS (Pons, 2006), MTCLIM logic/DAYMET (Thornton et al., 2021, 1997; Thornton and Running, 1999), METEOLAND (De Cáceres et al., 2018) or *r.sun* for GRASS/QGIS (Hofierka et al., 2002) are some examples of this.

Some of the aforementioned models employ the upward-looking hemispherical viewshed algorithm. The viewshed algorithm is a virtualized version of hemispherical canopy photography (Kodysh et al., 2013). Three main results are obtained from them: i) global, ii) direct and iii) diffuse radiation. Regardless of the version of the upward-looking hemispherical viewshed algorithm employed, two parameters control the algorithm: i) atmosphere transmissivity and ii) diffuse radiation rate. Transmissivity is a property of the atmosphere and is the quotient between the radiation received at the top of the atmosphere and that reaching the earth's surface, ranging from 0 (no transmission) to 1 (complete transmission). Typically observed values are 0.6–0.7 for very clear sky conditions and 0.5 for a generally clear sky. The percentage of global radiation that is diffused is approximately 0.2 for very clear sky conditions and 0.7 for very cloudy sky conditions. (ArcGis Help, 2022), (Kodysh et al., 2013). It should be noted that transmissivity and diffuse radiation rate depend on atmospheric conditions and are constantly changing. Not only cloud cover but also precipitation, dust, or aerosol presence attenuate the amount of diffuse and direct solar radiation for a given surface. Hence, transmissivity and diffuse radiation rate are time-space-specific and they are constantly changing. To consider this attribute consistent with a feasible computational effort, the following method was applied: for the 2022-year, 365 different grid maps of potential radiation PR (one for each DOY) were obtained using the upward-looking hemispherical viewshed algorithm and assuming values of transmissivity and diffuse radiation rate for the very best clear sky conditions (0.6 and 0.2 respectively). For each day we want to obtain a radiation map, the ratio of the actual radiation Rs (registered for each weather station) to DOY-specific *PR* at the weather station location was calculated. These punctual *Rs/PR*-ratio values were then spatially interpolated using the splines-with-tension method (Mitášová and Mitáš, 1993) obtaining an *Rs/PR* grid-cell map. Then, a daily *Rs* grid-cell map was derived by multiplying this *Rs/PR* ratio grid and the *PR* grid. In this work, *Solar Analyst* for ArcGIS environment was employed in order to obtain the 365 DOY-specific *PR* maps and *v.surf.rst* for GRASS environment to interpolate daily *Rs/PR*-ratio values using the splines-with-tension method. A monthly radiation average map was aggregated using the same method for the monthly-basis calculations. Further details about those algorithms can be found in the aforementioned references and GIS platform's user manuals.

2.5. Sensitivity analysis of PM56-ETo to the meteorological variables

In order to assess the sensitivity of the ETo to the meteorological variable changes, a sensitivity analysis was developed. In this analysis, all the meteorological variables except one were maintained constant on the average monthly values while the ETo was calculated using the minimum and the maximum value of the range of each variable. The difference between them (ΔETo %) is expressed as a percentage of the ETo for the average conditions. This sensitivity analysis methodology has been widely employed in the literature for the very same purpose (Goyal, 2004; Irmak et al., 2006; Paturel et al., 1995; Vicente-Serrano et al., 2014; Wang et al., 2011; Xu et al., 2006).
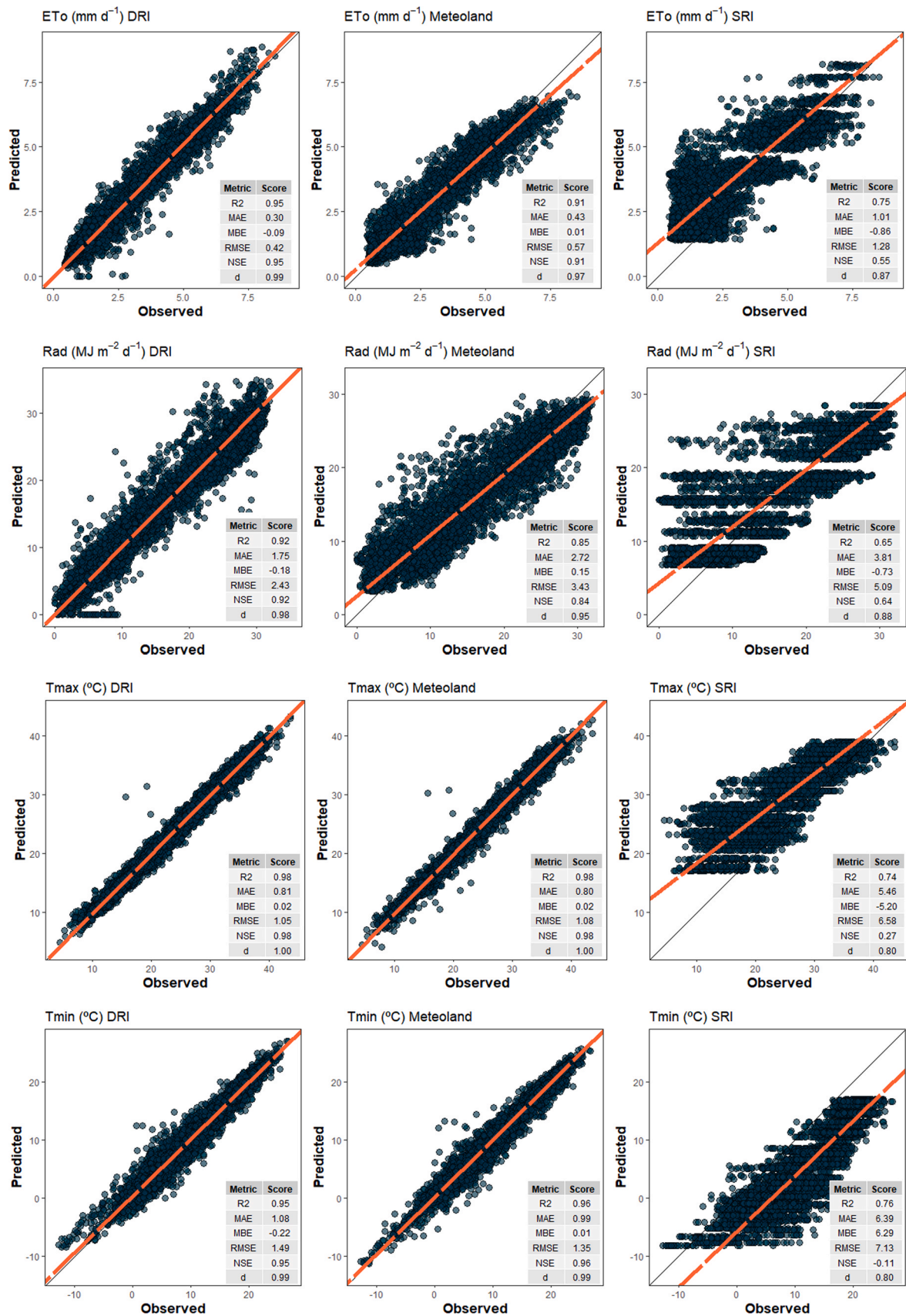
Fig. 5. Predicted vs Observed plot integrating all the validation stations. R2 = Coefficient of determination; MAE = Mean absolute error; MBE = Mean bias error; RMSE = Root mean squared error; d = Willmott Index of Agreement; NSE = Nash and Sutcliffe Nash-Sutcliffe model efficiency.
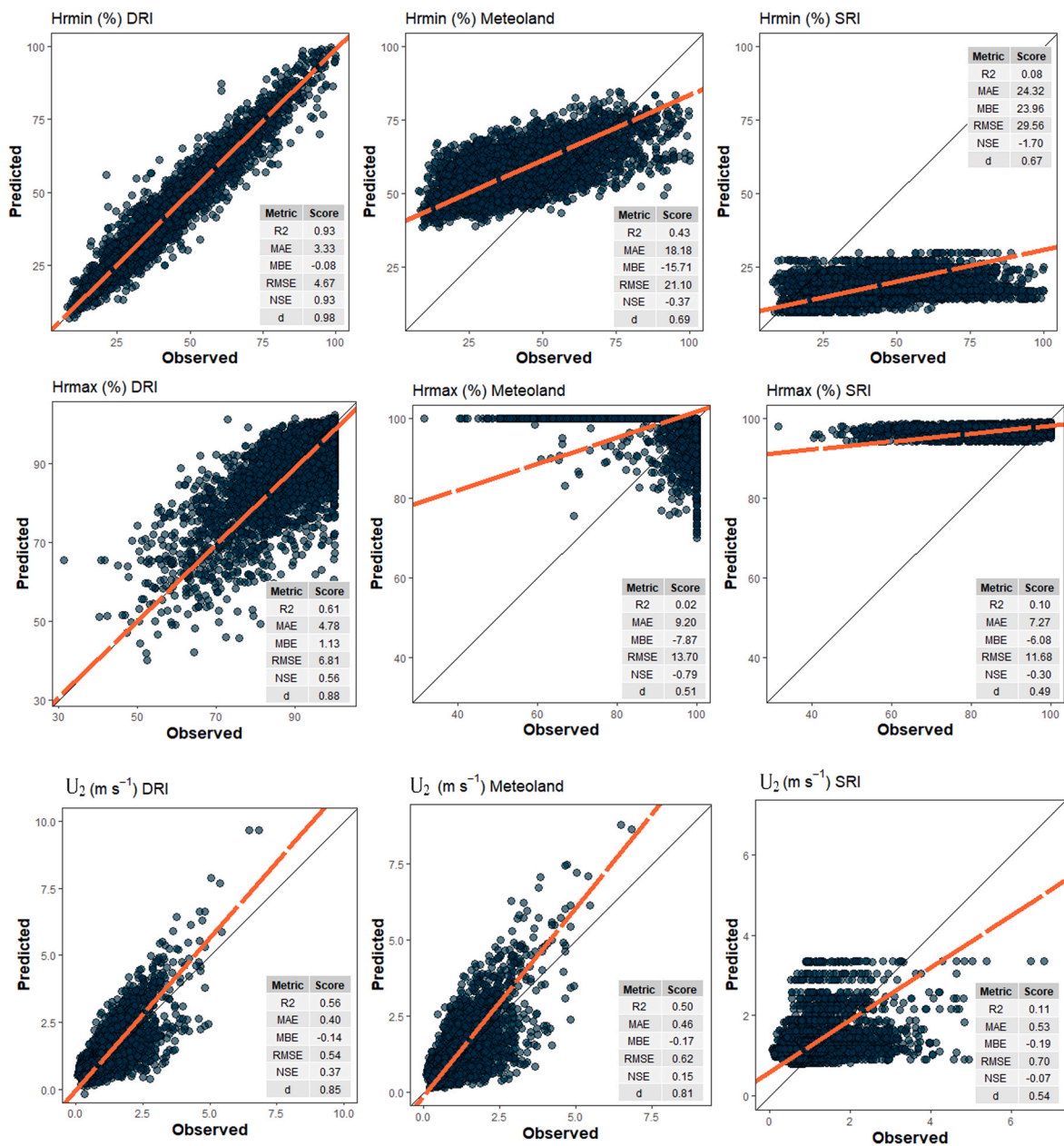
Fig. 5. (*continued*).

2.6. Maps validation and model performance

The accuracy of the interpolated maps has to be assessed by comparing modeled vs actual registered data in other weather stations different from the one employed in the interpolation procedure. For this purpose, 20% of the AWN stations (14 out 63) were randomly selected to be employed only for the validation tests, as shown in Fig. 2. As explained before, the rest of the stations (49 out 63) were employed exclusively in the interpolation procedures.

A number of statistical metrics can be found in the literature with the aim of assessing the ability of models to capture reality. According to Legates and McCabe (1999), a model performance assessment should include one or several absolute/relative error measures and one or several goodness-of-fit measures. Taking into account that the square of deviations (e.g., root mean square error, *RMSE*) use to be more sensitive to outliers than deviations ($P_j - O_j$) in an absolute value sense (e.g., mean absolute error, *MAE* or mean bias error, *MBE*), the statistical metrics included in Table 2 were employed to assess the ETo maps.

As regards the performance comparison between models, two dimensionless indices were calculated: i) Willmott index of agreement, *d*, (Willmott, 1981), and ii) Nash-Sutcliffe model efficiency, *NSE*, (Nash and Sutcliffe, 1970). *NSE* ranges between 1 and −∞. *NSE* = 1 means a perfect match between model outputs and observed values, and *NSE* < 0 means that the average of the observations would be a better predictor than the model output. Regarding the Wilmott index of agreement, *d* has limits of 0, indicating no agreement, and 1, indicating perfect agreement (Groenendijk et al., 2014).

The three evaluated models were graphically compared using a Taylor diagram (Taylor, 2001). The similarity between two patterns in the Taylor diagram is quantified in terms of their correlation, the amplitude of their variations -standard deviations-, and their centered root-mean-square difference. In the Taylor diagram, only one mark per model output is represented using the three dimensions. The closer the model mark regarding the "observed" mark is, the better the agreement was.

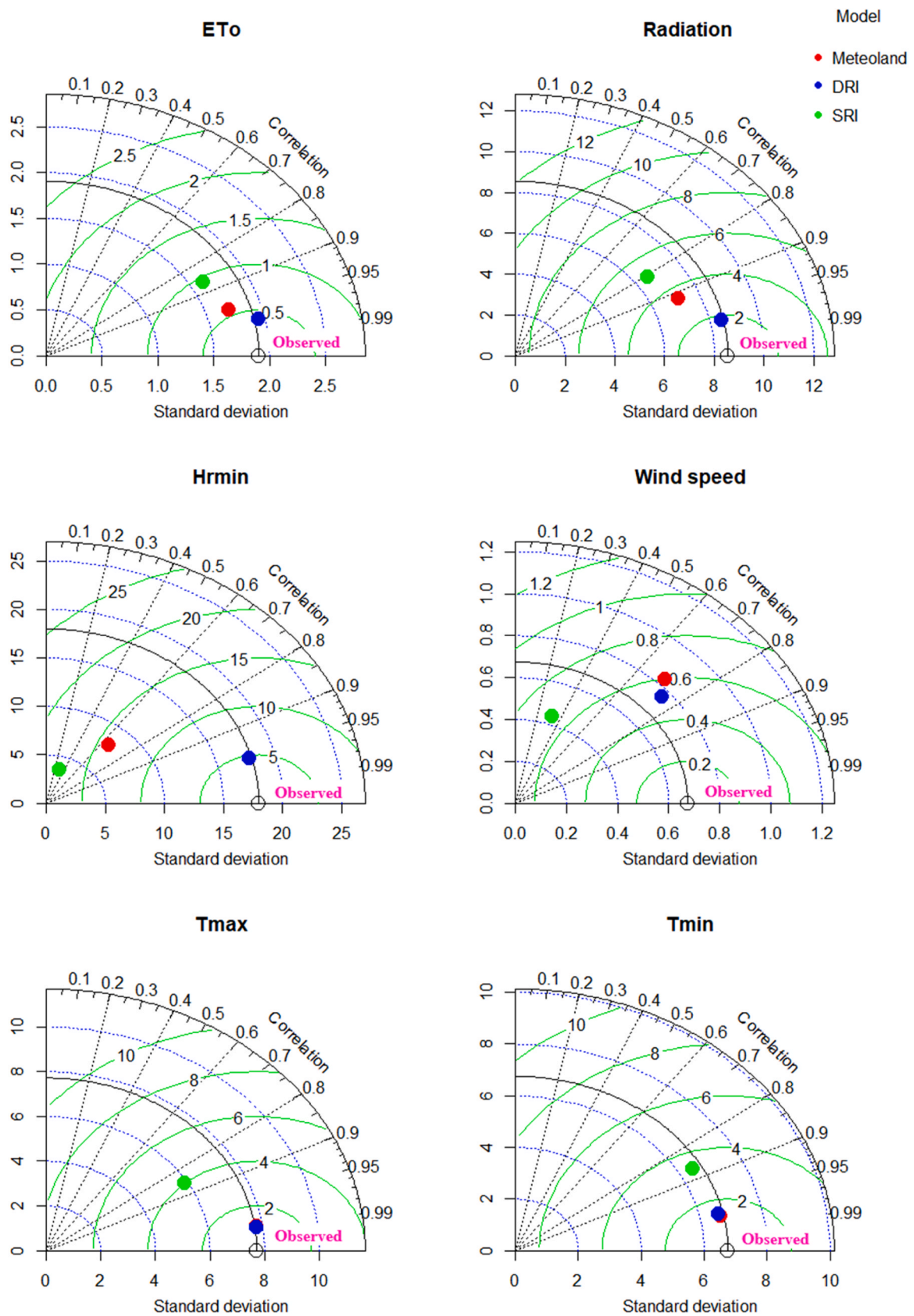Finally, the impact of using the DRI-interpolated vs nearest-weather-

Fig. 6. Taylor Diagram comparing the three interpolation procedures performance.
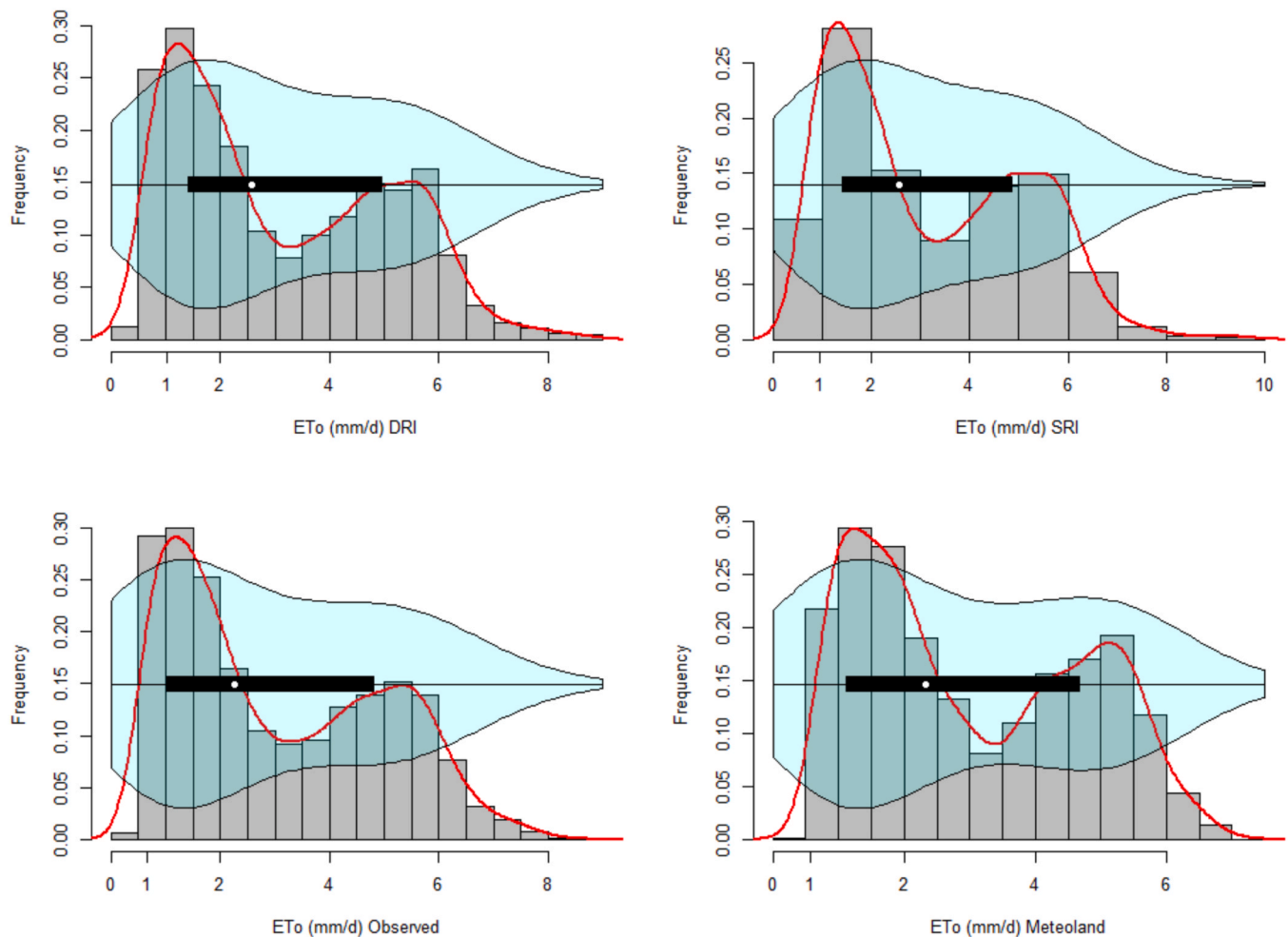
Fig. 7. Frequency histograms and violin plots for the observed and interpolated values or ETo.

station ETo value on a daily irrigation recommendation was assessed and quantified as follows: The area that is closest to each JRs-weather-station was obtained by creating the Thiessen polygons (Fig. 10) for each weather station. On the other hand, the centroid of each individual plot or farm was obtained, and the DRI-ETo value from the interpolated maps was assigned to it. The total number of plots in the JRs was 263,413. The difference between the DRI-interpolated and the recorded in the nearest weather station ETo value was computed for each plot and compared.

3. Results and discussion

3.1. Interpolation procedures performance assessment

The final purpose of this paper was to develop a dynamic method of mapping ETo. At the end of each day, a programmed script could pro-duce a new continuous surface of PM56-ETo using the registered data of an AWN. However, since the proposed method does not make a direct spatial interpolation of ETo values but requires one interpolated surface of each meteorological variable involved in the PM56-ETo equation, not only the ETo maps should be assessed. In order to understand how the different methods worked out, *Rs, Tmax, Tmin, HRmax, HRmin*, and U_2 maps in addition to reference evapotranspiration were compared. The validation of the maps was developed by comparing the map value in those grid-cells where 14 out 63 stations (see Fig. 2) not included in the interpolation process were located, to the actual values registered in those stations.

For each meteorological variable (Fig. 5), a predicted vs observed scatter plot was generated, including all the validation weather stations and all the daily observations of the year 2022 ($365 \times 14 = 5110$). A legend with the statistical metrics was also incorporated in the body of the scatter plot. SRI showed the worst performance in all statistical metrics and for all meteorological variables, demonstrating that static regressions method based on historical data did not accurately capture the variability of daily ETo in respect of the monthly averaged values they come from. At the other end, the best performance was encountered for the DRI procedure.

DRI and Meteoland exhibited a similar performance for Tmax and Tmin and relatively close for Rs. However, Meteoland showed a poor performance in Hrmin, Hrmax, and U_2. This aspect was transmitted to the final ETo results and was reflected on the metrics, producing an R^2 of 0.95 vs 0.91, *NSE* of 0.95 vs 0.91, and *d* of 0.99 vs 0.97, for DRI and Meteoland respectively. A lesser error was also obtained according to the metrics for DRI as well.

Another way of comparing models' performance is by means of the Taylor Diagram. The similarity between patterns in this graphical method is quantified in terms of their correlation, amplitude of their variations -standard deviations-, and their centered root-mean-square difference. Each model is represented in the body of the plot using those three coordinates. The closer a point in respect of the point rep-resenting the actual observed values is, the better performance the model has. Similar results to the one obtained using the statistical metrics could be observed in this analysis. The advantage of this graph over other performance evaluation methods, is that it allows

Table 3

Synthetic 2022-year with one day per month and daily-average-conditions PM56 ETo (AB09 weather station). ETo=reference evapotranspiration; Tmax=maximum temperature; Tmin=minimum temperature; HRmax=maximum relative humidity; HRmin=minimum relative humidity; U_2 =wind velocity; Rs= incident solar radiation.

DOY	Rs	Rs (MJ m^{-2} d^{-1}) From	To	Tmax	Tmax (°C) From	To	Tmin	Tmin (°C) From	To	Hr max	HRmax (%) From	To	Hr min	HRmin (%) From	To	U_2	U_2 (m s^{-1}) From	To	Average conditions ETo (mm d^{-1})
15	9.79	5.21	12.81	12.61	8.47	20.48	-2.54	-7.72	3.83	95.29	75.10	100.00	43.72	9.71	67.04	1.09	0.46	2.70	1.01
46	12.02	2.92	16.99	15.41	9.40	21.10	0.94	-3.54	7.08	92.05	68.77	100.00	40.04	12.84	76.60	1.24	0.60	2.48	1.69
74	9.95	2.73	19.26	12.52	7.94	18.05	5.28	-1.14	9.80	95.26	89.60	99.10	63.70	30.12	90.60	2.27	0.59	4.71	1.66
105	19.78	2.09	28.84	16.23	4.43	24.69	4.37	-4.39	9.47	94.71	85.70	99.10	47.87	20.29	81.20	1.56	0.68	3.64	2.94
135	27.72	14.09	31.12	26.75	15.09	33.30	9.52	5.76	14.18	89.94	77.90	97.70	28.03	14.75	65.52	1.21	0.61	2.13	5.11
166	28.68	12.82	31.29	33.03	26.73	40.17	13.69	10.52	18.41	80.20	58.89	94.40	18.53	10.56	27.71	1.08	0.65	2.13	6.04
196	28.85	18.45	30.94	36.43	30.37	39.96	17.64	14.97	22.18	81.88	55.88	98.40	18.03	9.70	41.53	1.45	0.71	2.27	6.88
227	25.57	12.76	28.77	34.67	28.98	38.57	17.00	12.05	20.46	90.21	72.20	100.00	20.42	12.29	34.56	1.56	0.63	2.65	6.07
258	19.17	4.76	24.81	28.52	21.05	36.38	13.26	7.01	18.81	88.69	65.01	100.00	30.83	17.34	70.60	1.08	0.61	2.06	3.76
288	12.78	2.79	20.22	25.66	19.98	30.50	11.24	3.90	16.43	95.92	81.00	100.00	36.48	13.56	66.24	1.17	0.54	2.15	2.50
319	9.34	3.82	14.33	17.60	11.31	24.27	5.74	-1.47	13.30	95.15	75.40	100.00	50.87	17.68	86.30	1.39	0.42	3.14	1.38
349	6.00	1.44	10.48	14.31	9.93	20.51	5.55	-0.68	13.10	98.24	88.20	100.00	68.79	37.10	89.00	1.32	0.38	3.16	0.80

Table 4

Sensitive analysis of ETo to Tmax, Tmin, HRmax, HRmin, Rs and U_2 changes in 2022-year (AB09 weather station). ETo=reference evapotranspiration; Tmax=maximum temperature; Tmin=minimum temperature; HRmax=maximum relative humidity; HRmin=minimum relative humidity; U_2 =wind velocity; Rs= incident solar radiation.

DOY	Δ ETo (%)	ETo (mm d^{-1}) when Rs was Min	Max	Δ ETo (%)	ETo (mm d^{-1}) when Tmax was Min	Max	Δ ETo (%)	ETo (mm d^{-1}) when Tmin was Min	Max	Δ ETo (%)	ETo (mm d^{-1}) when HRmax was Min	Max	Δ ETo (%)	ETo (mm d^{-1}) when HRmin was Min	Max	Δ ETo (%)	ETo (mm d^{-1}) when U_2 was Min	Max	Average conditions ETo (mm d^{-1})
15	0.00	1.03	1.03	50.73	0.86	1.38	1.09	1.01	1.03	-6.98	1.07	1.00	-45.68	1.28	0.82	85.41	0.71	1.58	1.01
46	27.48	1.39	1.85	37.59	1.39	2.03	4.66	1.66	1.74	-7.10	1.78	1.66	-39.13	1.96	1.30	47.39	1.37	2.17	1.69
74	59.88	1.23	2.22	31.67	1.44	1.97	8.64	1.58	1.73	-5.80	1.72	1.63	-60.14	2.22	1.22	27.12	1.43	1.88	1.66
105	74.92	1.49	3.69	50.16	2.18	3.65	11.89	2.74	3.09	-2.67	3.00	2.92	-26.86	3.30	2.50	18.58	2.74	3.29	2.94
135	37.26	3.59	5.49	34.33	4.06	5.82	5.29	5.00	5.27	-1.22	5.15	5.08	-10.03	5.23	4.71	19.41	4.68	5.67	5.11
166	38.31	4.05	6.37	22.56	5.44	6.81	3.90	5.96	6.19	-0.81	6.06	6.02	-1.34	6.07	5.99	26.21	5.54	7.13	6.04
196	23.83	5.52	7.15	16.37	6.19	7.32	2.74	6.82	7.01	-1.72	6.95	6.83	-4.60	6.94	6.63	26.53	5.97	7.79	6.88
227	32.20	4.51	6.46	18.52	5.43	6.56	2.42	6.00	6.15	-1.94	6.15	6.03	-4.65	6.17	5.88	34.14	5.04	7.11	6.07
258	52.89	2.33	4.32	31.69	3.23	4.42	6.08	3.66	3.89	-2.84	3.83	3.72	-12.24	3.86	3.40	30.26	3.36	4.49	3.76
288	45.68	1.84	2.98	27.21	2.15	2.83	3.27	2.47	2.55	-3.36	2.56	2.48	-23.32	2.74	2.16	43.67	2.03	3.12	2.50
319	11.59	1.30	1.46	45.26	1.12	1.75	4.29	1.37	1.43	-9.69	1.49	1.36	-59.34	1.77	0.95	72.63	0.95	1.96	1.38
349	0.00	0.82	0.82	38.61	0.69	1.00	6.80	0.79	0.84	-8.89	0.87	0.79	-70.16	1.15	0.58	64.34	0.59	1.11	0.80

Table 5

Effect of each meteorological variable on ΔETo %. - ≤ 10%, 10%<X ≤ 20%, 20%<XX≤ 30%, XXX> 30%. Tmax=maximum temperature; Tmin=minimum temperature; HRmax=maximum relative humidity; HRmin=minimum relative humidity; U$_2$ =wind velocity; Rs= incident solar radiation.

Month	Rs	Tmax	Tmin	HRmax	HRmin	U$_2$
	AB09 Weather Station					
January	-	XXX	-	-	XXX	XXX
February	XX	XXX	-	-	XXX	XXX
March	XXX	XXX	-	-	XXX	XX
April	XXX	XXX	X	-	XX	X
May	XXX	XXX	-	-	-	X
June	XXX	XX	-	-	-	XX
July	XX	X	-	-	-	XX
August	XXX	X	-	-	-	XXX
September	XXX	XX	-	-	-	XXX
October	XXX	XX	-	-	X	XXX
November	X	XXX	-	X	XXX	XXX
December	-	XXX	-	X	XXX	XXX
Month	Average Validation Weather Stations					
January	-	XXX	-	-	XXX	XXX
February	XX	XXX	-	-	XXX	XXX
March	XXX	XXX	-	-	XXX	XXX
April	XXX	XXX	-	-	XX	XX
May	XXX	XXX	-	-	X	X
June	XXX	XX	-	-	-	-
July	XXX	X	-	-	-	-
August	XXX	X	-	-	-	-
September	XXX	XX	-	-	X	X
October	XXX	XX	-	-	X	X
November	-	XXX	-	X	XXX	XXX
December	-	XXX	-	X	XXX	XXX

understanding at a glance how far one model is from the actual data and from the other models they are being compared. In Fig. 6 can be seen the Taylor Diagrams of the ETo and the different meteorological variables involved in the interpolation procedures. Fig. 6 was plotted using "plotrix" R package (Lemon, 2006). Another additional aspect can be seen in this graph: when two models exhibit similar values of correlation and error, the standard deviation breaks the tie. The standard deviation of the observed values is represented with a solid black line along the graph. The closer the point is in respect to this line, the better, because this is a symptom of the similarity of probability distributions. As can be seen in Fig. 6, SRI showed the worst performance and DRI the best one. In those meteorological variables with similar behavior when DRI and Meteoland were compared, always DRI was closer to the standard deviation line.

As was mentioned in the last paragraph, the shape of the distribution function between observed and modeled values is also important. For this purpose, in the Fig. 7 both, a frequency histogram (with its density function), and overlapped, violin plots were generated for observed, DRI, SRI and Meteoland values of ETo. The violin plot (Adler et al., 2022) is a symmetric representation of a box-and-whiskers plot. A similar shape in those three plots guarantees a similar distribution of probability. As can be seen in Fig. 7, DRI was able to reproduce, with greater similarity than the other methods, the shape of the observed-ETo distribution.

3.2. Sensitivity analysis of PM56-ETo

In order to understand the behavior of the different interpolation procedures, a sensitivity analysis of the PM56 ETo to the different meteorological variables involved was developed for the year 2022 in the AB09 validation station (see Fig. 2). This station was selected because it is located just in the center of the JRs. First of all, average values of *Tmax, Tmin, HRmax, HRmin, Rs* and *U$_2$* on a monthly basis were calculated and assigned to the 15th day of the month. On the other hand, each month's minimum and maximum absolute values of each variable were recorded, indicating the range of this variable in this month. Results were exposed in Table 3. In this table, the first column on the left indicates the day of the year (DOY) for each 15th day of each month. Following this in the first row, 9.79 MJ m^2 d^{-1} is the monthly average value of *Rs* for January and occupies the second column, and finally, 5.21 MJ m^2 d^{-1} and 12.81 MJ m^2 d^{-1} is the range of *Rs* for the same month that can be seen in the third and fourth columns. Next columns are showing the same information for the rest of the meteorological variables. To finish with, the last column shows the daily-average-conditions PM56 ETo (mm d^{-1}) obtained for this synthetic 2022-year with only one day per month.

Emulating the same structure of Table 3, results of the sensitivity analysis were summarized in Table 4. In this analysis, all the meteorological variables except one were maintained constant on the average monthly values exposed in Table 3. Then, the ETo was calculated using the minimum and the maximum value of the range of each variable, and the difference between them (ΔETo %), expressed as a percentage of the ETo for the average conditions, pointed out in Table 4. Thus, for the first raw, when *Rs* adopted the minimum value in January, ETo was 1.03 mm d^{-1}(third column), exactly the same when *Rs* adopted the maximum value (fourth column), being 0% the increment of the ETo produced. The next columns are showing the same information for the rest of the
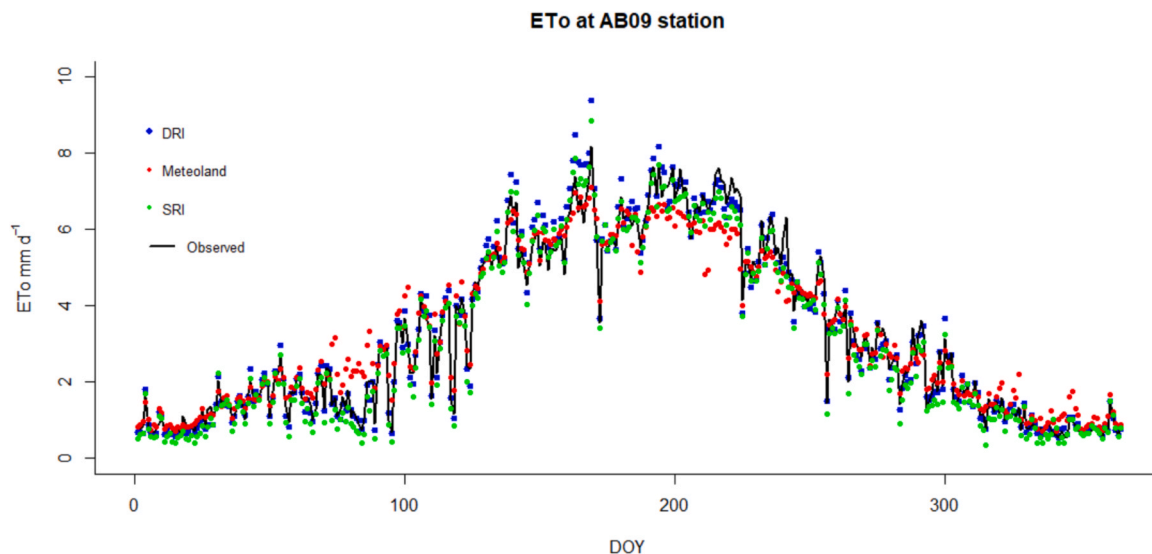

Fig. 8. Observed and DRI, SRI and Meteoland ETo for the year 2022 in the AB09 validation station.

Table 6

Regression equation coefficients of DRI for Tmax, from DOY 150 to DOY 156. Tmax = Maximum temperature, LONG = Longitude, in degrees; LAT = Latitude, in degrees; MEDIT = Distance to the nearest sea with clear influence in the weather synoptic (the Mediterranean Sea in our case), in m; RAD = Annual average incoming solar radiation, in MJ d-1; RADx = Annual average incoming solar radiation, in MJ d-1, within xi, where x is a radius of 2.5, 5, and 25 km; ELEV = Elevation, in m; ELEVx = Mean elevation, in m, within xi, where x is a radius of 2.5, 5, and 10 km; Slope = Terrain slope, in %; Aspect =Terrain aspect, in 0–360 degrees, with respect north (0 degrees).

DOY	Variable	Constant	ELEV	LONG	LAT	MEDIT	RAD	RAD2.5	RAD5	RAD25	ELEV2.5	ELEV5	ELEV10	Aspect	Slope
150	Tmax	12.5312				-0.000015	-1.1087		2.0733		0.0005		-0.0050	0.0053	
151	Tmax	102.7047	0.0045		-1.5592	0.0000103	-0.9204	-0.4759	0.6207						
152	Tmax	81.8164	0.0136	-0.3742	-1.9658					1.2970	-0.0128		-0.0124	0.0026	
153	Tmax	57.6764	0.0122		-1.8185	0.00000182				2.3012				0.0007	
154	Tmax	80.4191	0.0029		-1.0594		-0.8430	-0.1860	0.2880					0.0008	
155	Tmax	64.4761			-1.0303				0.4509			0.0099	-0.0090	0.0008	
156	Tmax	38.5027	-0.0058				-0.9199	0.6105			-0.0061	0.0072		0.0020	-0.1198

meteorological variables. This sensitivity analysis methodology has been widely employed in the literature for the very same purpose (Goyal, 2004; Irmak et al., 2006; Paturel et al., 1995; Vicente-Serrano et al., 2014; Wang et al., 2011; Xu et al., 2006).

Based on the results of Table 4, Table 5 summarize the effect of each meteorological variable on ETo. The first part of the table is referred to the AB09 weather station we used as an example, and the second part is the result of averaging ΔETo (%) for all the validation weather stations prior to calculating Table 5. Only significant differences were encountered in wind velocity (U_2). According to this, changes in *Rs* has no effect on ETo in winter, a slightly effect in summer, but a deep influence in spring, summer and autumn. *Tmax* has a slightly effect in summer, but a high influence in the rest of the year. *HRmin* demonstrated capacity to modify ETo in autumn and winter, and finally, U_2 showed a high or very high influence on ETo although this depends on the wind exposure of the area. The station AB09 showed a deep influence to wind in summer, however the average of the validation weather station showed a low influence in summer. *Tmin* and *HRmax* had no influence at all to modify the ETo. Fig. 8 shows the complete ETo values of the year 2022 for the validation station AB09. According to the Table 5, and taking into account the good performance of both, Meteoland and DRI for *Rs* and *Tmax*, we can conclude that the meteorological variable responsible of the deviations between observed and modeled ETo values (Fig. 8) is the wind velocity. New investigations have to be done in this field to improve the accuracy of this interpolation.

3.3. Daily Dynamic (DRI) vs Monthly Static (SRI) Regression-Based Interpolation comparison of Tmax, Tmin, Hrmax, Hrmin, U2

As was explained before, SRI and DRI, from a mathematical sight, are the same interpolation procedure. The SRI-procedure produces only once the regression equations from historical data (one equation per meteorological variable and per month), and they are utilized every day to generate new maps. That is why we called this method "static". However, in DRI, using exactly the same process, a new regression equation is obtained every day. According to the atmospheric conditions of each day, different geographical features are able to explain spatial variability. DRI adapts to the synoptic pattern of that day using some geographical features or others as appropriate to explain the spatial variability. For the year 2022, 365 days x 6 meteorological variables = 2190 regression equations were generated. In order to illustrate how the procedure worked, in Table 6 we reproduced the regression equation coefficients of 7 consecutive days for *Tmax*. It is worth emphasizing how the geographical features involved are constantly changing from one day to another. It can be checked that the behavior was always exactly like that for all the variables and all the days of the year, and that is why we call this method "dynamic". This capacity of adaptation to the synoptic pattern is undoubtedly the best quality of that method and the cause of the good results.

3.3. Radiation Rs interpolation procedure

Many efforts can be found in the literature addressing how to produce radiation maps (Dubayah and Rich, 1995; Fu and Rich, 2000; Wilson and Gallant, 2000; Miklánek, 1993; Pons, 2006; Thornton et al., 1997, 2021; Thornton and Running, 1999; De Cáceres et al., 2018; Hofierka et al., 2002). Those algorithms solve precisely the amount of radiation that reaches at the top of the atmosphere one specific DOY, the effect of the relief in the actual amount that reaches the soil, and, when the real atmospheric parameters are known, the effect of the atmosphere. All the uncertainty of this method is related to those parameters (transmissivity and diffuse radiation rate) because they depend on the cloud cover, precipitation, dust or aerosols presence, etc., that use to be constantly changing. In addition, those parameters are not registered for the AWN. In this work, to overcome this, a simple but effective method was applied. Each DOY, a map of potential radiation was generated
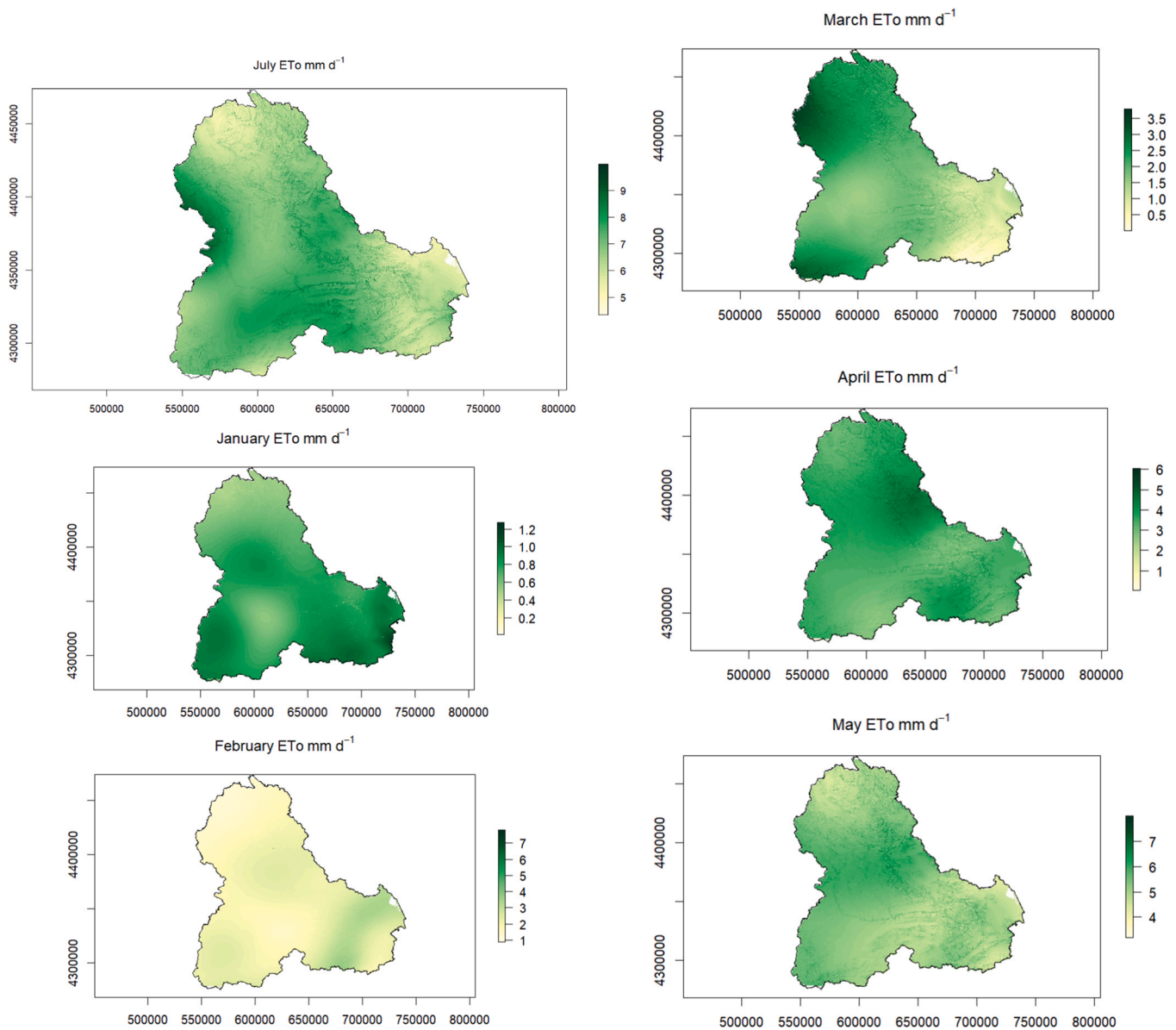
Fig. 9. PM56 ETo maps in the JRs for the 15th day of each month for the year 2022. Zoom made to the July map. Notice the detailed resolution in areas with important relief.

using the best clear conditions, using a commercial software. Then, using the registered data of radiation Rs, each day at each weather stations a Rs/PR-ratio was obtained and spatially interpolated. This way the real effect of the atmosphere in the radiation was spatially accounted for. Rs maps were compared to a contrasted method, and a better performance was encountered. Again, the proposed method can be called "dynamic" because using the registered data at the AWN, is able to adapt to the synoptic pattern.

3.4. Final DRI PM56 ETo maps

In this study, 365 maps of PM56 ETo for the JRs were obtained. To illustrate the final product, the corresponding map to the 15th day of each month of the year 2022 were plotted and can be seen in Fig. 9.

3.5. Impact of using the DRI-interpolated vs nearest-weather-station ETo value on a daily irrigation recommendation

For this purpose, the landscape of the JRs was divided into enclosures that "belong to each weather station" using the Thiessen's polygon method as can be seen in Fig. 10. For the 15th day of each month of the year 2022 and for each Thiessen polygon, the ETo registered in the weather station was compared to the DRI-interpolated ETo value corresponding to each individual plot. To do this, the centroid of each individual plot or farm was obtained, and the DRI-ETo value from the interpolated maps was assigned to it, and then compared to the one registered at the weather station.

Table 7 summarizes that comparison. Due to the extension of that table, only one month was included (June) after checking that results are representative of the rest of the year. The DRI-ETo range into each Thiessen polygon was obtained was calculated by subtracting the maximum and the minimum values and expressed as absolute value (mm) and relative value (%) respectively.
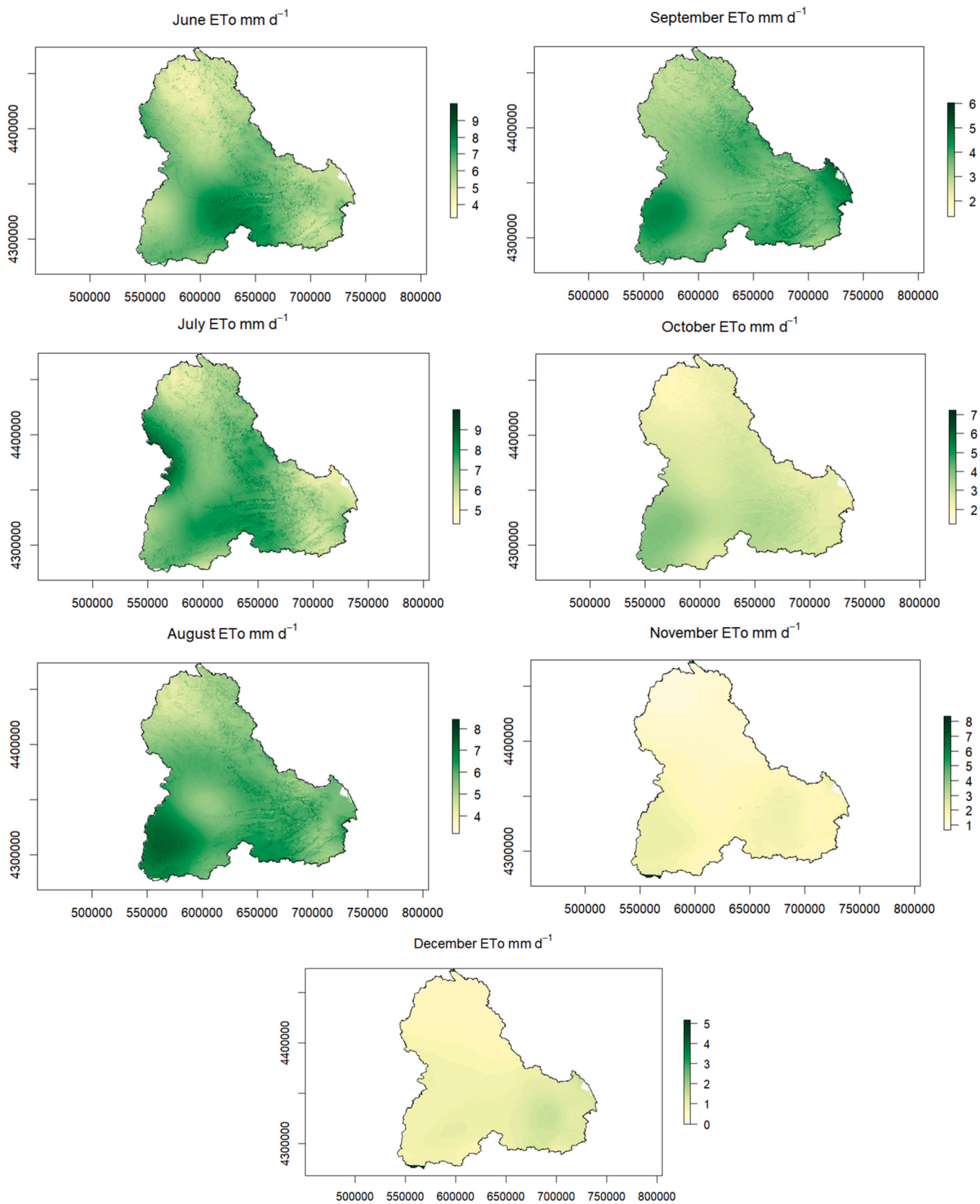
Fig. 9. (*continued*).

Taking into account that crop water needs -according to FAO-56 methodology- use to be calculated as ETc = ETo x Kc, (being ETc the crop evapotranspiration, and Kc the crop coefficient), and thus a linear combination of ETo, the very same deviation observed when the nearest weather station ETo value is employed instead of the site-specific interpolated value, is expected to be transferred to the water needs.
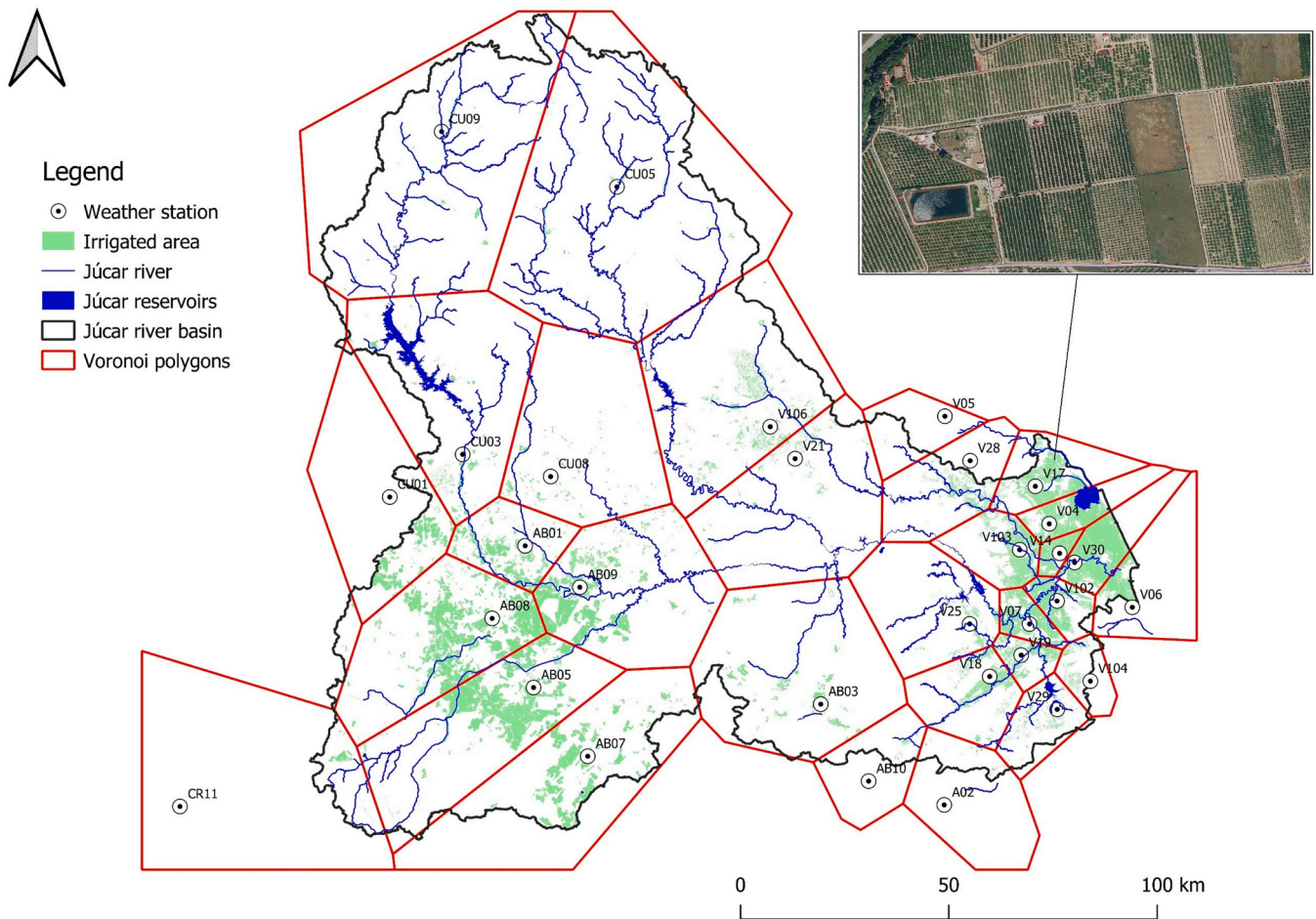
Fig. 10. Thiessen polygon's landscape division for the SIAR weather network.

The mean value of that difference for the entire JRs was 9.14% for the year 2022 employed as a demonstrative example throughout this entire work, but with punctual values reaching more than 30%. This reveals the necessity of using an interpolation method capable to adapt the synoptic pattern of each day, producing site-specific values of ETo for each farm. Using the nearest weather station value of ETo must be overcome.

4. Conclusions

Several targets were set prior to begin with this investigation; however, the germ was a purely practical objective: to develop a dynamic method of mapping ETo that could be used to produce site-specific irrigation recommendations. At the end of each day, a programmed script could produce a new continuous surface of PM56-ETo using the registered data of an AWN. However, as the work progressed, a second objective was gaining weight: contributing to an improved comprehension of the ETo mapping on a daily basis considering the geographical characteristics of the landscape. Our study was conducted in the Jucar River system, a Mediterranean region of eastern Spain where the intensive irrigated agriculture and a pronounced relief in certain areas, provided an excellent context to address this problem. On the one hand we had the necessity of generating ETo maps, and on the other, a proper geographical context.

Based on an existing statistical interpolation procedure developed to work on a monthly basis (DRI), a new version adapted to work on a daily basis (DRI) was developed. With the only aim to know the quality of the results, both, existing and proposed algorithms were compared to a contrasted interpolation method (Meteoland). Using performance model assessment statistics demonstrated that the interpolation method originally planned to work monthly, was unable to produce proper maps of any meteorological variable nor ETo. DRI exhibited a similar performance than Meteoland for *Tmax* and *Tmin* and a better performance in the rest of meteorological variables. Both models demonstrated a poor performance in U_2. On the other hand, a very simple but effective method to interpolate R_s was proposed, and demonstrating a very good performance.

Both, DRI and R_s interpolation methods, we called them "dynamic" methods because of their capacity of adapt to the synoptic pattern of each day, being without any doubt the best quality of them and the cause of the good results. Besides, DRI was the only method that had the ability of reproducing the shape of the observed-ETo distribution.

Deviations between observed and modeled ETo values could be attributed to the low performance mapping the wind speed. Although the quality of the ETo maps produced is very high, new investigations have to be done in this field to improve the accuracy of the wind velocity interpolation. This would be especially important in windy areas where the potential influence of U_2 on ETo has been demonstrated could be very high.

The impact of using the nearest-weather-station ETo vs DRI-interpolated value on a daily irrigation recommendation was investigated and near 10% average value of error was encountered for the whole JRs in the year 2022.

Declaration of Competing Interest

The authors declare that they have no known competing financial interests or personal relationships that could have appeared to influence

Table 7

DRI-ETo site-specific by plot vs nearest-weather-station registered ETo value for the 15th of June 2022 comparison. ETo = Reference evapotranspiration, DRI = Dynamic Regression-Based Interpolation, SIAR = Acronym of the agricultural weather network.

Weather Station	SIAR ETo (mm)	All plots average DRI-ETo (mm)	Nº Plots	Maximum DRI-ETo (mm)	Minimum DRI-ETo (mm)	DRI-ETo Range (mm)	SIAR vs DRI (mm) average difference	SIAR vs DRI (%) average difference
A02	6.55	5.73	426	6.19	5.31	0.89	0.82	12.52
AB01	7.16	6.84	2723	7.52	6.23	1.30	0.32	4.49
AB03	7.27	7.22	3390	8.28	6.38	1.90	0.05	0.71
AB05	7.51	6.85	6920	9.04	6.08	2.95	0.66	8.76
AB07	6.97	6.71	1958	7.86	5.61	2.25	0.26	3.74
AB08	6.42	6.19	5390	7.50	5.20	2.30	0.23	3.53
AB09	6.19	7.81	5222	9.98	6.91	3.08	1.62	26.24
AB10	6.64	5.87	522	7.06	5.60	1.46	0.76	11.51
CR11	7.54	6.88	715	8.79	6.05	2.74	0.66	8.79
CU01	6.74	6.10	800	6.78	5.16	1.61	0.65	9.60
CU03	6.29	6.63	1703	7.56	5.92	1.64	0.34	5.40
CU05	5.13	5.28	12,958	7.83	4.31	3.52	0.15	2.87
CU08	6.20	6.06	1817	7.97	4.66	3.32	0.13	2.13
CU09	4.64	4.93	3829	9.45	3.86	5.60	0.29	6.20
V04	5.45	5.41	17,042	6.92	5.17	1.75	0.04	0.74
V05	4.99	5.90	284	7.60	5.58	2.02	0.91	18.16
V06	5.35	5.51	7815	8.05	5.14	2.91	0.16	2.92
V07	4.76	5.72	22,964	9.54	5.29	4.25	0.96	20.14
V102	6.05	5.84	17,265	8.53	5.52	3.01	0.21	3.46
V103	6.16	5.76	22,243	7.14	5.14	2.00	0.40	6.45
V104	6.61	6.00	4186	8.13	5.34	2.79	0.61	9.19
V106	6.54	6.52	8893	8.23	5.59	2.64	0.02	0.33
V14	5.59	5.62	13,774	5.93	5.35	0.58	0.03	0.62
V17	4.89	5.21	21,151	6.44	4.84	1.60	0.32	6.51
V18	5.08	5.15	11,379	6.60	4.60	2.01	0.07	1.36
V19	5.36	5.50	12,697	7.49	4.92	2.58	0.14	2.62
V21	6.34	6.63	4049	8.94	5.61	3.33	0.29	4.63
V25	5.05	5.78	9029	9.52	4.97	4.55	0.73	14.48
V28	5.04	5.27	10,741	7.27	4.82	2.44	0.23	4.54
V29	5.57	5.33	4517	6.79	4.94	1.85	0.24	4.36
V30	4.97	5.53	26,949	7.97	5.21	2.76	0.56	11.22

the work reported in this paper.

References

Adler, D., Kelly, S.T., Elliott, T., Adamson, J., 2022. vioplot violin plot.

Agnew, M.D., Palutikof, J.P., 2000. GIS-based construction of baseline climatologies for the Mediterranean using terrain variables. Clim. Res 14, 115–127. https://doi.org/10.3354/CR014115.

Allen, R.G., Pereira, L.S., Raes, D., Smith, M., 1998. Crop evapotranspiration: guidelines for computing crop water requirements. Irrigation and Drainage Paper 56. FAO, Rome.

Brown, P.W., 2007. Use of the ASCE Standardized Reference ET Equation by Agricultural Weather Networks in the Western U.S.: Current Status and Future Challenges. Examining the Confluence of Environmental and Water Concerns - Proceedings of the World Environmental and Water Resources Congress 2006 1–10. https://doi.org/10.1061/40856(200)256.

CHJ. Confederación Hidrográfica del Júcar, 2022. Plan hidrológico de la demarcación hidrográfica del Júcar: ciclo de planificación hidrológica 2022 – 2027. First ed.

Ministerio de Agricultura, Alimentación y Medio Ambiente, València, Spain (in Spanish).

Daly, C., Gibson, W.P., Taylor, G.H., Johnson, G.L., Pasteris, P., 2002. A knowledge-based approach to the statistical mapping of climate. Clim. Res 22, 99–113. https://doi.org/10.3354/CR022099.

De Cáceres, M., Martin-StPaul, N., Turco, M., Cabon, A., Granda, V., 2018. Estimating daily meteorological data and downscaling climate models over landscapes. Environ. Model. Softw. 108, 186–196. https://doi.org/10.1016/j.envsoft.2018.08.003.

Dubayah, R., Rich, P.M., 1995. Topographic solar radiation models for GIS. Int. J. Geogr. Inf. Syst. 9, 405–419. https://doi.org/10.1080/02693799508902046.

Elliott, R.L., Hubbard, K.G., Brusberg, M.D., Hattendorf, M.J., Howell, T.A., Marek, T.H., Snyder, R.L., 2000. The role of automated weather networks in providing evapotranspiration estimates. National irrigation symposium. Proceedings of the 4th Decennial Symposium, Phoenix, Arizona, USA, November 14–16, 2000. 243–250.

Fu, P., Rich, P.M., 2000. The Solar Analyst, 1.0 Manual. Helios Environmental Modeling Institute (HEMI, USA.

Garnier, B.J., Ohmura, A., 1968. A method of calculating the direct shortwave radiation income of slopes. J. Appl. Meteor. Clim. 7, 796–800. https://doi.org/10.1175/1520-0450(1968)007<0796:AMOCTD>2.0.CO;2.

Goyal, R.K., 2004. Sensitivity of evapotranspiration to global warming: a case study of arid zone of Rajasthan (India. Agric. Water Manag 69, 1–11. https://doi.org/10.1016/J.AGWAT.2004.03.014.

Groenendijk, P., Heinen, M., Klammler, G., Fank, J., Kupfersberger, H., Pisinaras, V., Gemitzi, A., Peña-Haro, S., García-Prats, A., Pulido-Velazquez, M., Perego, A., Acutis, M., Trevisan, M., 2014. Performance assessment of nitrate leaching models for highly vulnerable soils used in low-input farming based on lysimeter data. Sci. Total Environ. 499, 463–480. https://doi.org/10.1016/J.SCITOTENV.2014.07.002.

Hodam, S., Sarkar, S., Marak, A.G.R., Bandyopadhyay, A., Bhadra, A., 2017. Spatial Interpolation of Reference Evapotranspiration in India: Comparison of IDW and Kriging Methods. J. Inst. Eng. (India): Ser. A 98, 511–524. https://doi.org/10.1007/S40030-017-0241-Z.

Hofierka, J., Suri, M., others, 2002. The solar radiation model for Open source GIS: implementation and applications, in: Proceedings of the Open Source GIS-GRASS Users Conference. pp. 51–70.

Hungerford, R.D., Nemani, R.R., Running, S.W., Coughlan, J.C., 1989. MTCLIM: a mountain microclimate simulation model. Research Paper - US Department of Agriculture, Forest Service.

Irmak, S., Payero, J.O., Martin, D.L., Irmak, A., Howell, T.A., 2006. Sensitivity analyses and sensitivity coefficients of standardized daily asce-penman-monteith equation. J. Irrig. Drain. Eng. 132, 564–578. https://doi.org/10.1061/(ASCE)0733-9437(2006)132:6(564).

Kodysh, J.B., Omitaomu, O.A., Bhaduri, B.L., Neish, B.S., 2013. Methodology for estimating solar potential on multiple building rooftops for photovoltaic systems. Sustain Cities Soc. 8, 31–41. https://doi.org/10.1016/J.SCS.2013.01.002.

Legates, D.R., McCabe, G.J., 1999. Evaluating the use of "goodness-of-fit" measures in hydrologic and hydroclimatic model validation. Water Resour. Res 35, 233–241. https://doi.org/10.1029/1998WR900018.

Lemon, J., et al., 2006. Plotrix: a package in the red light district of R. R. -N. 6, 8–12.

Mancosu, N., Snyder, R.L., Spano, D., 2014. Procedures to develop a standardized reference evapotranspiration zone map. J. Irrig. Drain. Eng. 140. https://doi.org/10.1061/(ASCE)IR.1943-4774.0000697.

Mardikis, M.G., Kalivas, D.P., Kollias, V.J., 2005. Comparison of interpolation methods for the prediction of reference evapotranspiration – an application in Greece. Water Resour. Manag. 19, 251–278. https://doi.org/10.1007/S11269-005-3179-2.

Martí, P., Zarzo, M., 2012. Multivariate statistical monitoring of ETo: a new approach for estimation in nearby locations using geographical inputs. Agric. Meteor. 152, 125–134. https://doi.org/10.1016/J.AGRFORMET.2011.08.008.

Martinez-Cob, A., 1996. Multivariate geostatistical analysis of evapotranspiration and precipitation in mountainous terrain. J. Hydrol. (Amst.) 174, 19–35. https://doi.org/10.1016/0022-1694(95)02755-6.

Martínez-Cob, A., Cuenca, R.H., 1992. Influence of elevation on regional evapotranspiration using multivariate geostatistics for various climatic regimes in Oregon. J. Hydrol. (Amst.) 136, 353–380. https://doi.org/10.1016/0022-1694(92)90018-Q.

Martínez-Lüscher, J., Teitelbaum, T., Mele, A., Ma, O., Frewin, A.J., Hazell, J., 2022. High-resolution weather network reveals a high spatial variability in air temperature in the Central valley of California with implications for crop and pest management. PLoS One 17, e0267607. https://doi.org/10.1371/JOURNAL.PONE.0267607.

McVicar, T.R., Van Niel, T.G., Li, L.T., Hutchinson, M.F., Mu, X.M., Liu, Z.H., 2007. Spatially distributing monthly reference evapotranspiration and pan evaporation considering topographic influences. J. Hydrol. (Amst.) 338, 196–220. https://doi.org/10.1016/J.JHYDROL.2007.02.018.

Miklánek, P., 1993. The estimation of energy income in grid points over the basin using simple digital elevation model. Ann. Geophys. 296–312.

Mitášová, H., Mitáš, L., 1993. Interpolation by regularized spline with tension: I. Theory and implementation. Math. Geol. 25, 641–655. https://doi.org/10.1007/BF00893171/METRICS.

Nash, J.E., Sutcliffe, J.V., 1970. River flow forecasting through conceptual models part I – a discussion of principles. J. Hydrol. (Amst.) 10, 282–290. https://doi.org/10.1016/0022-1694(70)90255-6.

Ninyerola, M., Pons, X., Roure, J.M., 2000. A Methodological approach of climatological modelling of air temperature and precipitation througH GIS techniques. Int. J. Clim. 20, 1823–1841. https://doi.org/10.1002/1097-0088.

Ninyerola, Miguel, Pons, X., Roure, J.M., 2007a. Monthly precipitation mapping of the Iberian Peninsula using spatial interpolation tools implemented in a Geographic Information System. Theor. Appl. Clim. 89, 195–209. https://doi.org/10.1007/S00704-006-0264-2.

Ninyerola, Miquel, Pons, X., Roure, J.M., 2007b. Objective air temperature mapping for the Iberian Peninsula using spatial interpolation and GIS. Int. J. Climatol. 27, 1231–1242. https://doi.org/10.1002/JOC.1462.

Noshadi, M., Sepaskhah, A.R., 2005. Application of geostatistics for potential evapotranspiration estimation. Iran. J. Sci. Technol., Trans. B: Eng. 29.

Paturel, J.E., Servat, E., Vassiliadis, A., 1995. Sensitivity of conceptual rainfall-runoff algorithms to errors in input data — case of the GR2M model. J. Hydrol. 168, 111–125. https://doi.org/10.1016/0022-1694(94)02654-T.

Pons, X., Ninyerola, M., 2008. Mapping a topographic global solar radiation model implemented in a GIS and refined with ground data. Int. J. Climatol. 28, 1821–1834. https://doi.org/10.1002/JOC.1676.

Pons X., 2006. Manual of miramon. Geographic Information System and Remote Sensing Software. Centre de Recerca Ecologica i Aplicacions Forestals (CREAF): Bellaterra, (http://www.creaf.uab.es/miramon).

Raes, D., Steduto, P., Hsiao, T.C., Fereres, E., 2009. Aquacrop-The FAO crop model to simulate yield response to water: II. main algorithms and software description. Agron. J. 101, 438–447. https://doi.org/10.2134/AGRONJ2008.0140S.

Shulski, M., Cooper, S., Roebke, G., Al Dutcher, 2018. The Nebraska Mesonet: technical overview of an automated state weather network. J. Atmos. Ocean Technol. 35, 2189–2200. https://doi.org/10.1175/JTECH-D-17-0181.1.

Taylor, K.E., 2001. Summarizing multiple aspects of model performance in a single diagram. J. Geophys. Res.: Atmospheres 106, 7183–7192. https://doi.org/10.1029/2000JD900719.

Thornton, P.E., Running, S.W., 1999. An improved algorithm for estimating incident daily solar radiation from measurements of temperature, humidity, and precipitation. Agric. Meteor. 93, 211–228. https://doi.org/10.1016/s0168-1923(98)00126-9.

Thornton, P.E., Running, S.W., White, M.A., 1997. Generating surfaces of daily meteorological variables over large regions of complex terrain. J. Hydrol. (Amst.) 190, 214–251. https://doi.org/10.1016/s0022-1694(96)03128-9.

Thornton, P.E., Shrestha, R., Thornton, M., Kao, S.C., Wei, Y., Wilson, B.E., 2021. Gridded daily weather data for North America with comprehensive uncertainty quantification. Sci. Data 2021 8:1 8, 1–17. https://doi.org/10.1038/s41597-021-00973-0.

Tovar-Pescador, J., Pozo-Vázquez, D., Ruiz-Arias, J.A., Batlles, J., López, G., Bosch, J.L., 2006. On the use of the digital elevation model to estimate the solar radiation in areas of complex topography. Meteorol. Appl. 13, 279–287. https://doi.org/10.1017/S1350482706002258.

Vicente-Serrano, S.M., Lanjeri, S., López-Moreno, J.I., 2007. Comparison of different procedures to map reference evapotranspiration using geographical information systems and regression-based techniques. Int. J. Climatol. 27, 1103–1118. https://doi.org/10.1002/JOC.1460.

Vicente-Serrano, S.M., Azorin-Molina, C., Sanchez-Lorenzo, A., Revuelto, J., Morán-Tejeda, E., López-Moreno, J.I., Espejo, F., 2014. Sensitivity of reference evapotranspiration to changes in meteorological parameters in Spain (1961–2011). Water Resour. Res 50, 8458–8480. https://doi.org/10.1002/2014WR015427.

Wang, W., Peng, S., Yang, T., Shao, Q., Xu, J., Xing, W., 2011. Spatial and temporal characteristics of reference evapotranspiration trends in the Haihe River Basin, China. J. Hydrol. Eng. 16, 239–252. https://doi.org/10.1061/(ASCE)HE.1943-5584.0000320.

Willmott, C.J., 1981. On the validation of models. Phys. Geogr. 2, 184–194. https://doi.org/10.1080/02723646.1981.10642213.

Wilson, J., Gallant, J., 2000. Terrain Analysis: Principles and Applications, Earth sciences. Geography.

Xu, C. yu, Gong, L., Jiang, T., Chen, D., Singh, V.P., 2006. Analysis of spatial distribution and temporal trend of reference evapotranspiration and pan evaporation in Changjiang (Yangtze River) catchment. J. Hydrol. 327, 81–93. https://doi.org/10.1016/J.JHYDROL.2005.11.029.